



# Label-free multiphoton microscopy of human skin: longitudinal studies capturing cell dynamics

ALEXANDER VALLMITJANA, AMANDA DURKIN, ALEXANDER DVORNIKOV, BELÉN TORRADO, KRISTEN M. KELLY, JESSICA SHIU, ANAND K. GANESAN, AND MIHAELA BALU\*

Beckman Laser Institute, University of California, Irvin, CA 92617, USA

\*mbalu@hs.uci.edu

**Abstract:** This study presents recent advances in an imaging platform developed by our lab, the fast large area multiphoton exoscope (FLAME), a microscope designed for clinical skin imaging. Its dual-scanning modality enables reliable, cellular-scale imaging of the same skin locations over extended time periods across areas up to 1 cm<sup>2</sup>. Enabling fluorescence lifetime imaging microscopy, this device, for the first time *in vivo*, allows detailed longitudinal tracking of cellular dynamics in human skin, such as responses to injury, significantly advancing the capabilities of dermatological research. By overcoming previous limitations in large-area, high-resolution skin imaging, FLAME opens new opportunities for monitoring therapy responses, tracking cellular dynamics, and understanding skin biology at the cellular level.

© 2025 Optica Publishing Group under the terms of the [Optica Open Access Publishing Agreement](#)

## 1. Introduction

Optical imaging technologies have significantly advanced clinical and biological research, enabling unprecedented insights into disease mechanisms and enhancing clinical diagnostics [1–6]. In skin imaging, multiphoton microscopy (MPM) is particularly noteworthy, as it offers high-resolution images based on label-free molecular contrast, facilitating the understanding of cellular and sub-cellular processes [7–18].

Despite significant advances, clinical MPM skin imaging has faced challenges in capturing high-resolution images over large areas beneath the skin surface. This limitation is particularly problematic in longitudinal clinical studies, where precise imaging of the same location over time is crucial for understanding disease progression and treatment response. Additionally, the ability to study intra-subject and inter-subject variability at the cellular level remains constrained by existing technologies, which limits the potential for personalized treatments and a deeper understanding of disease mechanisms. Few longitudinal MPM imaging studies on human skin have been reported, primarily observing treatment effects where precise location imaging was not critical [19,20], such as monitoring metabolic changes in vitiligo following treatment [21] or making use of temporary markers for precise registration [22].

Our group has recently reported on the development of our *fast, large area multiphoton exoscope* (FLAME), an MPM imaging device, optimized for rapid and effective clinical skin imaging [23]. FLAME generates macroscopic images (ranging from millimeters to centimeters) with microscopic resolution (0.5–1 μm) based on label-free molecular contrast (fluorescence intensity and lifetime). This study aims to explore the FLAME's potential as an efficient tool for cellular-level skin imaging in longitudinal clinical studies, leveraging its large field-of-view, high spatial resolution and fast scanning speed.

Key innovations of the FLAME include two *in vivo* scanning modes: a fast scanning mode that maps centimeter-scale areas with micron resolution, and a slower scanning mode that scans millimeter-scale areas with sub-micron resolution. These capabilities enable us to reliably return

to the same cellular location over extended periods. This has allowed us to capture both short and long-term *in vivo* dynamics in human skin for the first time, with high molecular contrast, thanks to FLAME's time-resolved fluorescence detection.

## 2. Methods

### 2.1. Dual scanning mode

The FLAME microscope is designed for *in vivo* imaging of human skin. To achieve stable coupling between the microscope and a patient's skin, we use a metallic ring with a microscopy coverslip placed inside the ring. The ring is attached to the skin using double-sided tape (Fig. 1(D)) and magnetically couples to a custom-designed stage, enclosing the objective, and maintaining consistent contact during imaging.

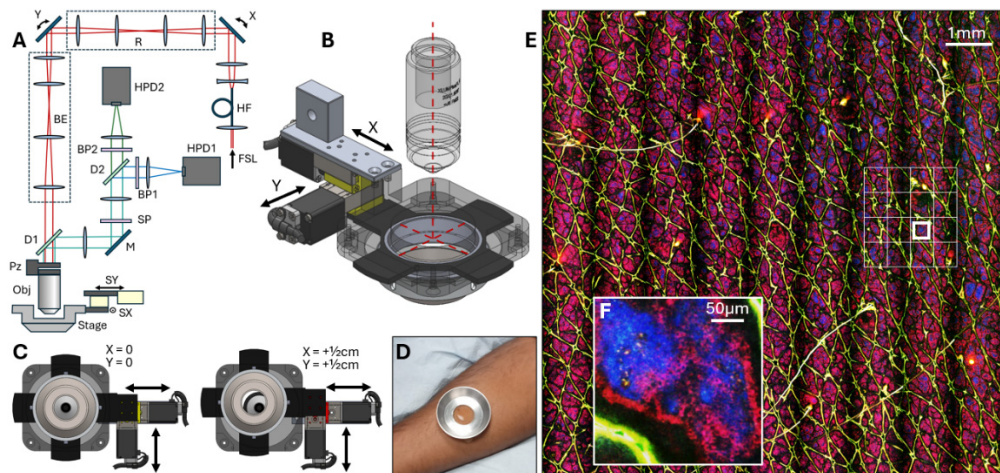


**Fig. 1. System overview and scanning modes of the FLAME microscope.** **A)** Optical path of the FLAME system. **B)** Close-up of the stage with the ability to push and pull the skin under the objective (objective has been moved upwards out of the way). **C)** View from beneath the objective, showing the centered stage (left) and the stage displaced (right). **D)** Image showing the metallic ring attached to a patient's arm. **E)** Large field of view ( $1\text{cm}^2$ ) image acquired via 9 stage-scanning strips (about  $1\text{\mu m}/\text{px}$ ). The image shows macroscopic features such as skin folds, furrows and wrinkles (green lines) as well as hairs. The  $4 \times 4$  grid shows the typical high-resolution area imaged via 16 raster scans (about  $500\text{ nm}/\text{px}$ ). **F)** Detail of a raster scan where single cells are observed: melanin-loaded keratinocytes and melanocytes of the basal layer (red) surrounding fibrillar collagen in the dermal papilla (blue). Abbreviations used in panel A: (FSL) femtosecond laser, (HF) hollow fiber, (X) resonant x-scanner, (R) relay lens set, (Y) galvo y-scanner, (BE) beam expander, (D) dichroic, (Pz) piezo mount, (Obj) objective, (SX) x-stage, (SY) y-stage, (M) mirror, (SP) short-pass, (BP) band-pass, (HPD) hybrid photomultiplier detector.

The FLAME uses a 4kHz resonant scanner (SC-30 EOPC) for fast axis scanning and a galvo scanner (QS10X-AG Thorlabs) for slow axis scanning. These scanning mirrors, combined with custom-designed relay and beam expander optics, along with a 20x, 1.05NA objective (XLUMPLFLN20XW Olympus) produce images with sub-micron resolution and an effective field of view of approximately  $1\text{mm}^2$  (Fig 1(A)). This configuration we call the raster scanning mode.

For imaging skin areas larger than  $1\text{ mm}^2$ , we engage a two-dimensional stage, powered by two independent motors (LSA10A-T4A Zaber). This stage is our custom design; a 3D-printed

mechanical translation unit that allows movement in the plane perpendicular to the optical axis around the objective (Fig. 1(B)). Since skin is highly elastic, movement of the stage attached to the skin through the metallic ring results in lateral displacement of the skin under the objective. This stage-scanning configuration enables *in vivo* imaging over skin areas up to 1cm<sup>2</sup> (Fig 1(C)). In this scanning modality, the Y galvo mirror is parked, and the resonant X scanner is used in combination with the stage movement along the Y-axis. This produces long strip images, where the short dimension corresponds to the 1 mm field of view of the objective and X resonant scanner, and the long dimension corresponds to the 1 cm range that the stage can drag the skin under the objective (Fig 1(E)). Because in this modality we drive the resonant scanner to a considerably wide angle (field of view of 1.1 mm), we observe the onset of vignetting in the X-axis. This manifests itself as vertical bands of decreased intensity in the edges of each strip (see Fig 1(E) and Fig 3(A)).

In a typical experiment, we first perform a single stage scan at an arbitrary depth (Fig 1(E)), which takes approximately 40s to image a 1cm<sup>2</sup> skin area at cellular resolution (1 μm/pixel). From this overview, using as reference macroscopic landmarks such as hair follicles, solar lentigines, nevi and other features, we identify regions of interest to perform the high-resolution resonant scans at sub-cellular resolution (Fig 1(F)). These raster-scanned images are diffraction limited, usually acquired as 1200px x 1200px images (yielding a field-of-view of 600 μm x 600 μm) in about 5s. The raster-scanned images can be acquired either as single field of view of up to 1 × 1 mm<sup>2</sup> or as mosaics over several square millimeters by engaging the stages to perform a ‘tile mosaic’, where adjacent fields of view are acquired and stitched together to form larger maps.

FLAME can also perform volumetric imaging by acquiring z-stacks of en-face images, achieved by moving the objective in the z-direction using a piezoelectric stage (P-725.4CDE2 PI) attached to the objective. While this z-stage has a 400 μm range, the effective depth penetration in human skin is typically limited to 150-200 μm, depending on the skin and lesion types, due to light attenuation and scattering.

Figure 1E shows a representative image captured at the dermal epidermal junction a volunteer’s forearm. This image illustrates FLAME’s capability to acquire *in vivo* images over a 1cm<sup>2</sup> area using stage scanning, as well as to obtain sub-cellular resolution images of smaller regions. The next section describes the color space selection for these images.

## 2.2. Spectral and fluorescence lifetime signal separation

The excitation source is an 80 MHz, 80fs pulse laser at 785 nm (Calmar). Fluorescence is recorded with two hybrid photodetectors (R11322U-40-01 Hamamatsu), split by a 506 nm dichroic (FF506-Di03 Semrock). This spectral split was selected such that the second harmonic generation signal from fibrillar collagen, along with the much dimmer but spatially resolvable NAD(P)H signal, are detected together in one detector. Longer wavelength signals, primarily from melanin and keratin, are directed to the second detector. The signals of these detectors are sampled by a high-speed digitizer (2.7 GHz), synchronized to the laser clock. Photons are then time-correlated using an FPGA (vDAQ, MBF Bioscience) to generate pixel temporal photon histograms with 32 time bins spaced between laser pulse, yielding a temporal resolution of 390ps. Data acquisition is run by ScanImage software (MBF Bioscience).

The complex spectral and fluorescence lifetime data require postprocessing to generate pseudo-colored images that highlight the fluorescence signatures of the different components in the samples. In the standard imaging configuration, we acquire sequential 32 temporal bin images from each of the two detectors, resulting in an effective 64 channels per pixel. We also employ a single-shot configuration, in which 16 temporal channels are captured per detector, generating a single 32 channel image. Since these high-dimensional raw images are difficult to interpret directly, we apply a simplified color projection for visualization. To determine the best projection, we acquired a large set of data at different depths and featuring representative

features of human skin. The phasor transform of the temporal photon histograms in each channel allowed a dimensionality reduction [24] which we employed to reduce each spectral channel to a 2-dimensional space (Fig 2(B)). Principal component analysis was applied to the phasor-transformed data to identify the directions in the phasor space that carry the most variance. By selecting the first principal component in each channel, accounting for approximately 95% of the variance in the training set, we further reduced the dimensionality (Fig. 2(C)). Color-coding the pixels according to the values in this first principal component (Fig. 2(C) – color gradient) allowed us to generate spectral/lifetime images encoding for the most variability (Fig. 2(D)), which when combined, produce the images depicted throughout this paper (Fig. 2(E)).

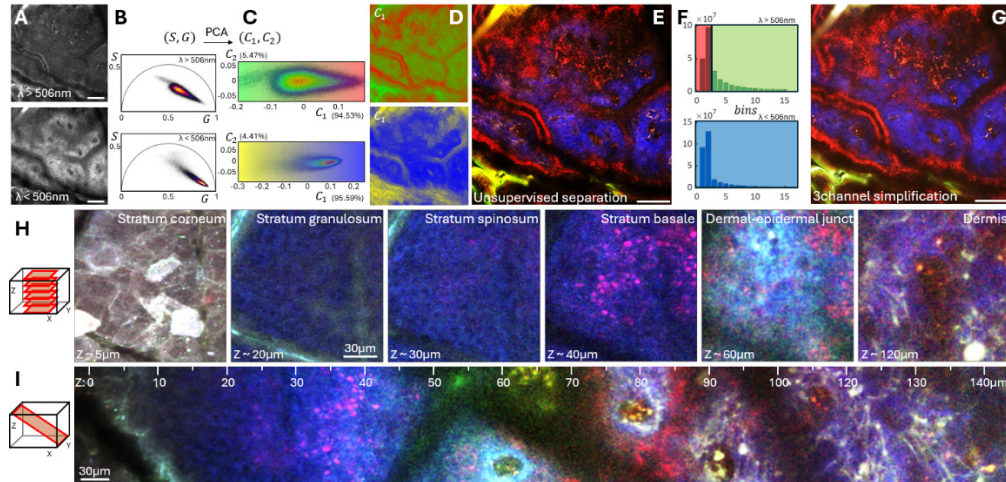


**Fig. 2. Reduction of high dimensional data into 3 channel images.** **A)** Images acquired by the two detectors of the FLAME microscope at the dermal-epidermal junction. **B)** Phasor plots of the fluorescence lifetime data corresponding to each detection channel. **C)** Principal component decomposition of the data, with a colormap proportional to the first component (capturing around 95% of the variance). **D)** Corresponding color-coded images based on the first principal component. **E)** Merged image obtained by the addition of the images in (A) multiplied by the colormaps in (C). **F)** Illustration of the alternative simplified approach, where the lifetime data is time-gated into two virtual channels for one detector. **G)** Image obtained by color-coding based on this alternative simplification which greatly resembles the image in (E). **H)** Sample z-slices of selected layers of the skin depicting the structures observed in this color projection. **I)** Oblique plane reconstructed from the z-stack intersecting all depths showing all structures in a continuum. Unlabeled scale bars are 100  $\mu\text{m}$ .

In this color scheme, red reflects shorter lifetimes in the longer spectral window (mainly corresponding to melanin), green indicates longer lifetimes in the same spectral window (mainly associated with keratin). Yellow arises from the balance between keratin to melanin content plus the contribution of other components. In the shorter spectral window, blue captures second harmonic generation from fibrillar collagen and yellow corresponds to longer lifetimes (mainly from NAD(P)H), while white indicates fluorescence signals present across all channels (mainly associated with elastin).

Because the raw files of these high-dimensional images are large and require a relatively high-photon yield, we employ a simplified configuration inspired by the above description when rapid visualization is necessary or when we choose not to save the data. In this method, we time-gate the data into 2 channels within the longer spectral window to obtain a coarse time separation. When chosen correctly, this produces images very similar to those generated from the full high-dimensional data. Specifically, we time gate the first 1/8<sup>th</sup> of the photon histogram

in the longer spectral channel and assign this portion the red color; the remaining 7/8 of the histogram is assigned green, while the entire shorter spectral detector is assigned blue (Fig. 2(F)). The resulting image (Fig. 2(G)) is remarkably similar to the image generated from the full high-dimensional space (Fig. 2(E)).

The combination of fluorescence lifetime and spectral signatures enables visualization of different cell types in distinct colors (Fig. 2(H) and Fig. 2(I)). Corneocytes at the surface appear as white polygonal structures, shifting toward teal tones as the signal becomes more dispersed and the keratin signal dominates. Epidermal keratinocytes appear blue (from the NAD(P)H signal), larger in the stratum granulosum and smaller in the stratum spinosum. Skin folds and hair follicles, both rich in keratin, appear green, while sebum-filled pores take on yellow tones. Melanin-loaded cells in the stratum basale appear red due to the short fluorescence lifetime of melanin. Cyan arises from second harmonic generation of fibrillar collagen in the dermal papilla, transitioning to a deeper blue where isolated fibrillar collagen is present in the dermis. The broad emission spectrum of elastin makes the fibers appear white, while isolated cells are seen in orange.

### 2.3. Imaging on human subjects

The results presented in this manuscript were obtained from two separate experiments. In the first experiment, we performed a longitudinal study by imaging the normal skin on the forearms of three volunteers over several weeks. This was done to assess our ability to repeatedly image the same location at a cellular-resolution. In the second experiment, we generated a wound model on a subject's skin and imaged the cellular dynamics 24 hours post-injury to demonstrate FLAME's capability of *in vivo* tracking of cellular dynamics within tissue as a proof-of-concept.

We created a wound model on a subject's thigh using a method inspired by a standard-of-care procedure for vitiligo treatment. In this procedure, small sheets of epidermis are harvested from a pigmented skin area and transplanted to the vitiligo-affected region. An epidermal harvesting device, CelluTome [25], was used for this in this case. The device gradually heats a small skin area, producing a matrix of  $2.5\text{mm}^2$  circular blisters. The epidermal roofs of the blisters are then sliced off for grafting. For our experiment, we discarded this graft tissue and instead imaged the exposed dermis beneath one of the generated blisters to capture the cellular immune response.

For the second experiment we developed custom scripts in MATLAB to analyze the time series. Motion artifacts were corrected using image correlation. First, the initial two frames were aligned by computing the x-y shift from the correlation required to register the second frame to the first. After this correction, their average was used as a reference to align the third frame. This process was repeated iteratively, so that for each new frame, the reference image used to calculate the shift included information from all previously corrected frames. Tracking of cells was performed in a semi-supervised fashion where a script was written to show a local area of all frames and the user could pinpoint the location of an object. Then the script would extract the x-y list of coordinates and save them as a trajectory for displacement calculation and plotting.

Both experiments were conducted with the full consent of all subjects under protocols approved by the Institutional Review Board for clinical research in human subjects at University of California, Irvine (HS# 2008-6307 for the first experiment and HS# 1909 for the second experiment).

## 3. Results

### 3.1. Consistent cellular-level localization

The FLAME instrument has unique capabilities for *in vivo* imaging of human skin. Its dual scanning modes, stage and raster scanning, enable acquisition of an overview image (stage-scan) before performing high-resolution imaging in a region of interest (raster-scan). The stage scan

generates near-cellular resolution images over a large field of view of  $1\text{cm}^2$ , and subsequently, the raster scan captures sub-cellular resolution, high-photon content images within a smaller area over several square millimeters. When performing successive imaging sessions, the operator can easily ensure that the instrument's placement errors remain within this  $1\text{cm}^2$  area. This ensures that the stage-scan image consistently includes recognizable landmarks (e.g. skin pores, hair follicles, specific skin fold patterns, etc.), maintaining precise localization across multiple sessions.

Once the landmark(s) are identified, they are used to pin-point the region of interest for the subsequent sub-cellular resolution raster scan imaging. The axial resolution of the instrument, determined by the optical components and excitation source, is approximately  $3\text{\mu m}$ . To ensure that successive imaging sessions target the same depth, we rely on cellular-scale landmarks such as elastin aggregates. This methodology allows us to reliably image the same locations at the cellular scale over time periods of months or even years.

Figure 3 illustrates this process. First, a stage-scan captures a large field of view (Fig. 3(A)) where, where a visible landmark – a ( $\sim 1\text{ mm}$ ) freckle – is identified. Then, a  $4 \times 4$  mosaic of raster-scans is performed around the region of interest (Fig 3(B)). For clarity, we show zoomed-in images at different depths (Fig 3(C)), revealing distinct layers such as *stratum-corneum*, -*spinosum*, -*basale*, and underlying dermis. Using this methodology, we were able to reliably re-image the same group of melanin-loaded cells at different time points over nearly a year, using a small elastin aggregate as reference for reliably location the same xyz position (Fig 3(D)), elastin aggregate in middle-left side). While these are from a single volunteer, we have consistently applied this method by re-imaging the same area with cellular resolution in two additional volunteers (see supplementary material, [Dataset 1 \[26\]](#)).

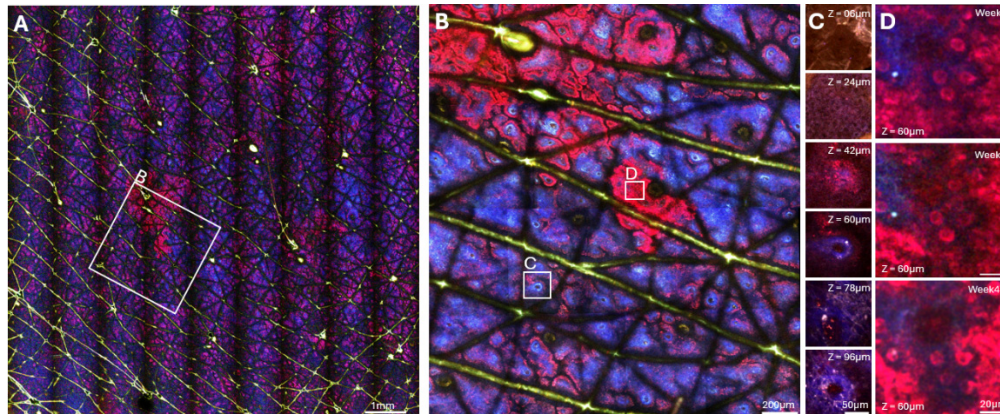


**Fig. 3. Tracking cells over long time scales.** **A)** Strip scan of a  $\sim 1\text{cm}^2$  field of view at the dermal-epidermal junction, where a  $\sim 1\text{mm}^2$  freckle is observed (9 strips, each  $1.1\text{ mm}$  wide, total  $9.9 \times 9.9\text{mm}^2$ ). **B)** Composition of  $4 \times 4$  resonant-galvo scans within the field of view at approximately the same depth ( $\sim 50\text{\mu m}$ ). **C)** Optical sections at 6 equidistant z-depths. **D)** Group of cells being followed over 47 weeks with a small elastin aggregate which was used for z-positioning.

### 3.2. Dynamic cellular imaging in human skin

FLAME's capability to reliably re-image the same location at cellular resolution enables detailed longitudinal studies of skin processes. This feature is crucial for understanding dynamic cellular behaviors over time, such as immune responses, wound healing, and tissue regeneration. Here we demonstrate a proof-of-concept application: capturing cellular dynamics in human skin in

response to skin injury. Specifically, we focus on the immune response following epidermal removal of blisters generated by using an epidermal harvesting device (see Methods).

Using FLAME's stage-scanning mode, we captured images of several circular blisters within the injured area 24 h post-injury (Fig 4(A)). We then imaged the exposed dermis beneath one of the blisters, acquiring a time series of frames every 45 seconds for 15 minutes. To ensure capturing motion in the vertical direction, each frame consisted of 6 slices separated by 2  $\mu\text{m}$ . Figure 4(B) depicts a still frame from the sequence with selected trajectories overlaid.

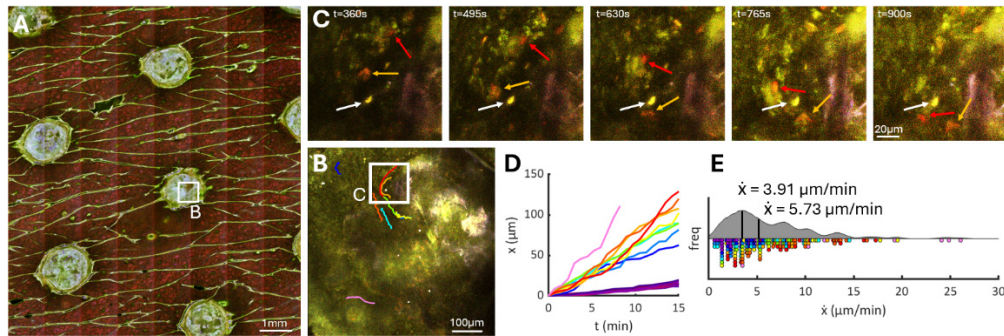


**Fig. 4. Tracking cells over short time scales.** **A)** Large field of view showing blister areas observed 24 h after injury. **B)** Still frame from a raster image sequence acquired from the exposed dermis beneath a blister, with select cell trajectories overlaid (white dots correspond to quasi-static trajectories). **C)** Insets of specific frames from the sequence, illustrating two cells being tracked (colored arrows indicate moving cells, white arrows mark static ones). **D)** Trajectories are plotted as linear displacement over time. Quasi-static trajectories are plotted in shades of purple for comparison. **E)** Storm plot displaying the distribution of the instantaneous speeds measured across all tracked trajectories (excluding static trajectories) with a median value of 5.73  $\mu\text{m}/\text{min}$  and a distribution mode at 3.91  $\mu\text{m}/\text{min}$ .

In the resulting movie (see supplementary material, [Visualization 1](#)) we observed clear motion of cells of varying sizes and spectral signatures against a background of static cells and connective tissue (Fig 4(C)). Cell dynamics were tracked using a custom script by first aligning frames via correlation to correct for motion artifacts and then segmenting cellular objects in each frame and associating them with detected objects in subsequent frames. This produced lists of 2-dimensional coordinates, which were used to plot displacement (Fig 4(D)) and depict instantaneous speed distributions in a storm plot (Fig 4(E)). The average speed measured was around 5  $\mu\text{m}/\text{min}$ , which appears to be too slow for vascular motion [27], we deduce corresponds to passive motion in interstitial fluid. One notable observation was an object with a velocity approximately double the group average, showing a mean speed of 13  $\mu\text{m}/\text{min}$  and peak values at 25  $\mu\text{m}/\text{min}$  (pink trajectory in Fig. 4).

### 3.3. Spectral and fluorescence lifetime cell signatures

The combination of FLAME's spectral configuration and fluorescence lifetime capabilities enables multiplexed separation of fluorescence signatures in our images. These signatures, along with the known skin structure and cellular morphology, allow us to distinguish different molecular components. Here we demonstrate the system's ability to detect and resolve the major molecular components in human skin. This approach lays the foundation for detailed characterization and monitoring of cellular responses and interactions *in vivo*.

As a proof of concept, we imaged three volunteers with different skin types (Fitzpatrick scales II, III and V) [28] by acquiring images at depths ranging from the surface to 150  $\mu\text{m}$  ( $1200 \times 1200 \times 30$  voxel volumes at  $0.5 \times 0.5 \times 5 \mu\text{m}$  voxel size). Using the high-dimensional raw

lifetime data of the two physical channels, we generated a UMAP [29,30] projection model using only a pre-segmented representative population of objects ( $\sim 10^4$  objects). This segmentation was performed using a watershed approach with a size and intensity stopping rule, to obtain the fluorescent signatures of all representative structures found across the skin. This trained UMAP model was then used to project every single pixel in the entire set of data ( $\sim 10^8$  pixels) to reduce the 32-dimensional space down to the 2-dimensional UMAP space. We were able to associate each of the main clusters identified in the UMAP projection with specific molecular components expected in the skin.

Inspection of images shows how subject 1 presented more elastin-rich areas in the dermis, characteristic to photodamage [31,32]. Subject 2 was imaged in a skin area dominated by the presence of a hair and deeper dermal layers, while subject 3 showed a high-melanin content in the basal layer and elongated rete ridges [33], that extended the presence of melanin-containing basal cells deeper into the dermis (Fig 5(A)). The UMAP projection of the pixels across all depths of these three subjects revealed many clusters which we were able to associate to the described characteristics above (Fig 5(B)). Subject 1 showed higher density in a cluster we associated to elastin, subject 2 displayed separated keratin and hair signal, and subject 3 exhibited enhanced density in clusters we associated to melanin and reduced density in the cluster we associated to fibrillar collagen. We confirmed the association of clusters to molecular components by plotting UMAP component 1 (horizontal in Fig. 5(B)) against skin depth, revealing the appearance of each signature in specific skin layers (Fig. 5(C)). Some clusters appear to be combinations of dispersed signals, such as skin folds revealing the keratin-heavy signature of the corneocytes in surface stratum corneum but at deeper levels. Additionally, certain clusters may be influenced by less abundant fluorescent molecules such as NAD(P)H and FAD present in cells [34].

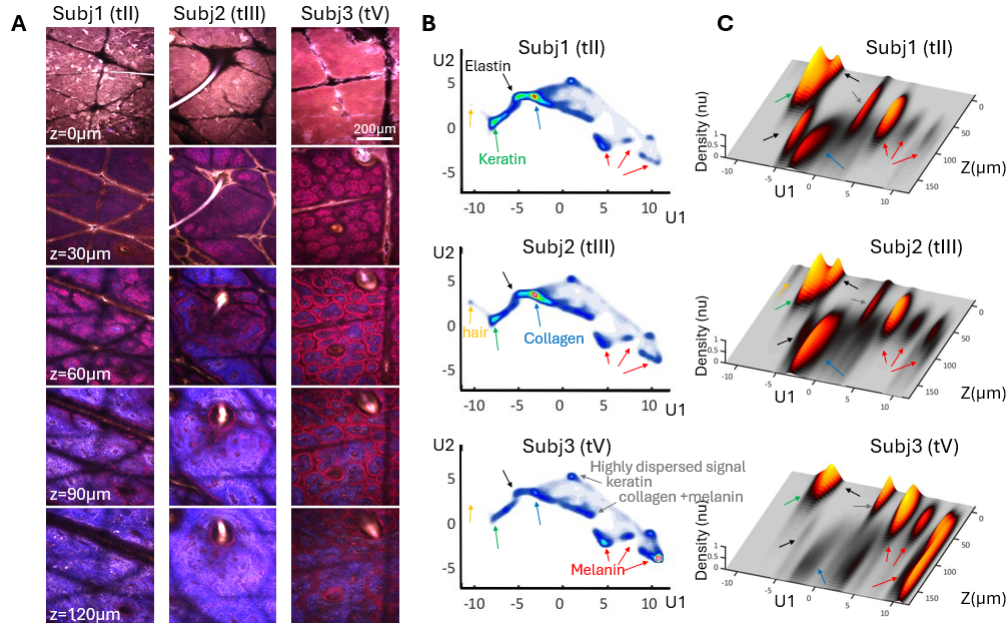


**Fig. 5. Identifying skin molecular components via their fluorescent signature.** **A)** Select images of three subjects imaged at increasing depths from skin surface. **B)** UMAP projection of all pixels in the imaged volumes of the three subjects reveals variability among subjects: e.g. increased elastin in subject 1 versus increased melanin in subject 3. **C)** Plotting UMAP component 1 versus imaging depth shows the same populations distributed unevenly in depth. Imaged volumes are  $1200 \times 1200 \times 52$  with a voxel size of  $0.5 \times 0.55 \times 5 \mu\text{m}$ .

#### 4. Discussion

In this manuscript we demonstrate FLAME's unique ability to reliably re-image the same physical locations  $\sim 1\text{mm}^2$  with cellular-scale accuracy over extended periods. This capability is enabled by the dual-scanning modality integrated into the FLAME imaging platform, which allows for 3D mapping of subsurface skin areas up to  $\sim 1\text{cm}^2$  with near-cellular resolution. Such functionality opens new opportunities for longitudinal dermatological studies. While strip scanning approaches have been previously reported for *ex vivo* imaging of human skin using MPM [23] and reflectance confocal microscopy (RCM) [35] implementing this technique for *in vivo* imaging has been challenging. This work represents the first successful application of this approach *in vivo* in clinical setting.

We have also demonstrated FLAME's ability to track cells in human skin over short and long-time scales, an advancement that is both novel and impactful. Long-term tracking can significantly enhance applications such as monitoring therapy responses and studying intra- and inter-subject variability at the cellular level. Short-term tracking of cellular dynamics will facilitate insights into rapid biological processes in skin. As a proof-of-concept, we captured cellular responses 24 h post-injury, representing the first *in vivo* visualization of cellular dynamics in human skin using fluorescence lifetime. While *ex vivo* studies have previously reported cellular dynamics in human skin [36], this work makes the first successful in-vivo demonstration in a human subject. We imaged cells moving at an average velocity of  $5\ \mu\text{m}/\text{min}$  within the injury site during the first 24 h post-injury. This velocity aligns with reported velocities of migrating neutrophils in response to inflammation in mouse models [37,38]. However, further investigation is needed to accurately interpret these cellular dynamics and determine cell speeds, as the highly motile cells appeared to be moving in interstitial lymphatic fluid trapped at the injury site. When combined with morphological and fluorescence lifetime signatures, along with their response times, this information is expected to potentially help identify specific cell types.

The label-free detection inherent in MPM imaging poses challenges in cell identification, requiring novel strategies to address this limitation. Our instrument, equipped with spectral and lifetime fluorescence discrimination, can resolve many diverse molecular signatures and shows potential to resolve low-photon yield signatures. We speculate that the separation we observe for the melanin signature (Fig. 5(BC)) could be due to different types of melanin, but this requires further investigation. The main limitation in MPM is its limited penetration depth, particularly in darker skin types, hindering the ability to capture the full cellular immune response. Another limitation of our current XY scanning approach is its susceptibility to involuntary patient motion, which can introduce spatial distortion during image acquisition. Some areas on the chest or the back are affected by vertical motion due to breathing and allow only single scan as opposed to averaging consecutive sequential scans. To address this, future work will explore the implementation of an X-Z-Y scanning strategy enabling vertical motion compensation, inspired by recent advances from other groups [39].

Despite the current limitations, FLAME's capabilities mark a significant advancement *in vivo* skin imaging, enabling detailed longitudinal studies and cellular tracking that were previously unachievable. Further improvements in depth penetration and label-free cell identification will enhance its utility, ultimately creating new opportunities for deeper insights into skin biology and more personalized dermatological treatments.

**Funding.** National Institute of Biomedical Imaging and Bioengineering (R01EB026705); National Institute of Arthritis and Musculoskeletal and Skin Diseases (R21AR082648); National Cancer Institute (R01CA259019); U.S. Department of Defense (HT94252311027); Skin Biology Resource-Based Center at the University of California, Irvine (P30AR075047); Chao Family Comprehensive Cancer Center (P30CA062203).

**Disclosures.** M.B. is a coauthor of a patent owned by the University of California, Irvine (UCI) related to the development of clinical MPM technology. Additionally, M.B. is a cofounder of Infraderm, LLC, a startup spin-off from UCI focused on commercializing clinical MPM imaging platforms that may benefit from the use of advanced analysis

tools. The Institutional Review Board and Conflict of Interest Office of UCI have reviewed patent disclosures and found no concerns.

**Data availability.** Raw images for all experiments are available on request and in (Dataset 1, Ref. [26]). Movie from which data for Figure 5 is available in the supplementary material (Visualization 1). MATLAB scripts for motion artifact correction, tracking and depicting trajectories is available on request.

## References

1. A. B. E. Attia, G. Balasundaram, M. Moothanchery, *et al.*, “A review of clinical photoacoustic imaging: Current and future trends,” *Photoacoustics* **16**, 100144 (2019).
2. L. Lin and L. V. Wang, “The emerging role of photoacoustic imaging in clinical oncology,” *Nat. Rev. Clin. Oncol.* **19**(6), 365–384 (2022).
3. G. Lentsch, E. G. Baugh, B. Lee, *et al.*, “Research Techniques Made Simple: Emerging Imaging Technologies for Noninvasive Optical Biopsy of Human Skin,” *J. Invest. Dermatol.* **142**(5), 1243–1252.e1 (2022).
4. B. W. Pogue, “Perspective on the optics of medical imaging,” *J. Biomed. Opt. Opt.* **28**(12), 121208 (2023).
5. H. Balasubramanian, C. M. Hobson, T. L. Chew, *et al.*, “Imagining the future of optical microscopy: everything, everywhere, all at once,” *Commun. Biol.* **6**(1), 1096 (2023).
6. N. T. Shaked, S. A. Boppart, L. V. Wang, *et al.*, “Label-free biomedical optical imaging,” *Nat Photonics* **17**(12), 1031–1041 (2023).
7. K. Koenig and I. Riemann, “High-resolution multiphoton tomography of human skin with subcellular spatial resolution and picosecond time resolution,” *J. Biomed. Opt.* **8**(3), 432 (2003).
8. S. Seidenari, F. Arginelli, C. Dunsby, *et al.*, “Multiphoton Laser Tomography and Fluorescence Lifetime Imaging of Melanoma: Morphologic Features and Quantitative Data for Sensitive and Specific Non-Invasive Diagnostics,” *PLoS One* **8**(7), e70682 (2013).
9. M. Balu, A. Mazhar, C. K. Hayakawa, *et al.*, “In vivo multiphoton NADH fluorescence reveals depth-dependent keratinocyte metabolism in human skin,” *Biophys. J.* **104**(1), 258–267 (2013).
10. M. Balu, K. M. Kelly, C. B. Zachary, *et al.*, “Distinguishing between benign and malignant melanocytic nevi by in vivo multiphoton microscopy,” *Cancer Res* **74**(10), 2688–2697 (2014).
11. M. Balu, C. B. Zachary, R. M. Harris, *et al.*, “In vivo multiphoton microscopy of basal cell carcinoma,” *JAMA Dermatol* **151**(10), 1068–1074 (2015).
12. J. Lin, I. Saknate, M. Valdebran, *et al.*, “Feature characterization of scarring and non-scarring types of alopecia by multiphoton microscopy,” *Lasers Surg. Med.* **51**(1), 95–103 (2019).
13. G. Lentsch, M. Balu, J. Williams, *et al.*, “In vivo multiphoton microscopy of melasma,” *Pigm. Cell Melanoma Res.* **32**(3), 403–411 (2019).
14. K. König, “Review: Clinical in vivo multiphoton FLIM tomography,” *Methods Appl. Fluoresc.* **8**(3), 034002 (2020).
15. G. Lentsch, M. Valdebran, I. Saknate, *et al.*, “Non-invasive optical biopsy by multiphoton microscopy identifies the live morphology of common melanocytic nevi,” *Pigm. Cell Melanoma Res.* **33**(6), 869–877 (2020).
16. M. Žurauskas, R. Barkalifa, A. Alex, *et al.*, “Assessing the severity of psoriasis through multivariate analysis of optical images from non-lesional skin,” *Sci. Rep.* **10**(1), 9154 (2020).
17. J. Shiu, L. Zhang, G. Lentsch, *et al.*, “Multimodal analyses of vitiligo skin identifies tissue characteristics of stable disease,” *JCI Insight* **7**(13), e154585 (2022).
18. M. Balu and B. Tromberg, “Multiphoton microscopy for non-invasive optical biopsy of human skin,” *Romanian Journal of Clinical and Experimental Dermatology* **2**(3), 160–166 (2015).
19. M. Balu, G. Lentsch, D. Z. Korta, *et al.*, “In vivo multiphoton-microscopy of picosecond-laser-induced optical breakdown in human skin,” *Lasers Surg. Med.* **49**(6), 555–562 (2017).
20. A. M. Pena, E. Decencière, S. Brizion, *et al.*, “In vivo melanin 3D quantification and z-epidermal distribution by multiphoton FLIM, phasor and Pseudo-FLIM analyses,” *Sci. Rep.* **12**(1), 1642 (2022).
21. J. Shiu, G. Lentsch, C. M. Polleys, *et al.*, “Noninvasive Imaging Techniques for Monitoring Cellular Response to Treatment in Stable Vitiligo,” *J. Invest. Dermatol.* **144**(4), 912–915.e2 (2024).
22. Y. Tian, Z. Wu, H. Lui, *et al.*, “Precise Serial Microregistration Enables Quantitative Microscopy Imaging Tracking of Human Skin Cells In Vivo,” *Cells* **13**(13), 1158 (2024).
23. A. Fast, A. Lal, A. F. Durkin, *et al.*, “Fast, large area multiphoton exoscope (FLAME) for macroscopic imaging with microscopic resolution of human skin,” *Sci. Rep.* **10**(1), 18093–14 (2020).
24. M. A. Digman, V. R. Caiolfa, M. Zamai, *et al.*, “The phasor approach to fluorescence lifetime imaging analysis,” *Biophys. J.* **94**(2), L14–L16 (2008).
25. S. N. Osborne, M. A. Schmidt, and J. R. Harper, “An Automated and Minimally Invasive Tool for Generating Autologous Viable Epidermal Micrografts,” *Adv Skin Wound Care* **29**(2), 57–64 (2016).
26. A. Vallmitjana, A. Durkin, A. Dvornikov, *et al.*, “Label-free imaging of in vivo skin: longitudinal studies capturing cell dynamics,” figshare (2025).<https://doi.org/10.6084/m9.figshare.30038206>.
27. L. An, J. Qin, and R. K. Wang, “Ultrahigh sensitive optical microangiography for in vivo imaging of microcirculations within human skin tissue beds,” *Opt. Express* **18**(8), 8220–8228 (2010).
28. T. B. Fitzpatrick, “Soleil et Peau,” *J. Med. Esthet.* **2**, 33–34 (1975).
29. L. McInnes, J. Healy, and J. Melville, “UMAP: Uniform Manifold Approximation and Projection for Dimension Reduction,” *arXiv* (2020).

30. C. Meehan, J. Ebrahimi, W. Moore, *et al.*, "Uniform Manifold Approximation and Projection (UMAP), MATLAB Central File Exchange," (2025).
31. E. F. Bernstein, V. Q. Chen, K. Tarnai, *et al.*, "Enhanced Elastin and Fibrillin Gene Expression in Chronically Photo-damaged Skin," *J. Invest. Dermatol.* **103**(2), 182–186 (1994).
32. S. Puschmann, C.-D. Rahn, H. Wenck, *et al.*, "Approach to quantify human dermal skin aging using multiphoton laser scanning microscopy," *J. Biomed. Opt.* **17**(3), 036005 (2012).
33. S. G. Lagarrigue, J. George, E. Questel, *et al.*, "In vivo quantification of epidermis pigmentation and dermis papilla density with reflectance confocal microscopy: Variations with age and skin phototype," *Exp Dermatol* **21**(4), 281–286 (2012).
34. T. P. L. Ung, S. Lim, X. Solinas, *et al.*, "Simultaneous NAD(P)H and FAD fluorescence lifetime microscopy of long UVA-induced metabolic stress in reconstructed human skin," *Sci. Rep.* **11**(1), 22171 (2021).
35. S. Abeytunge, Y. Li, B. Larson, *et al.*, "Rapid confocal imaging of large areas of excised tissue with strip mosaicing," *J. Biomed. Opt.* **16**(5), 050504 (2011).
36. F. E. Dijkgraaf, M. Toebe, M. Hoogenboezem, *et al.*, "Labeling and tracking of immune cells in ex vivo human skin," *Nat Protoc* **16**(2), 791–811 (2021).
37. D. B. Graham, B. H. Zinselmeyer, F. Mascarenhas, *et al.*, "ITAM signaling by Vav family rho guanine nucleotide exchange factors regulates interstitial transit rates of neutrophils in Vivo," *PLoS One* **4**(2), e4652 (2009).
38. B. H. Zinselmeyer, J. N. Lynch, X. Zhang, *et al.*, "Video-rate two-photon imaging of mouse footpad - A promising model for studying leukocyte recruitment dynamics during inflammation," *Inflamm. res.* **57**(3), 93–96 (2008).
39. Z. Wu, Y. Tian, J. Zhao, *et al.*, "Motion-tolerant 3D volumetric multimodality microscopy imaging of human skin with subcellular resolution and extended field-of-view," *Commun. Biol.* **8**(1), 186 (2025).